Multisensor Fusion with Hyperspectral Imaging Data: Detection and Classification

Su May Hsu and Hsiao-hua K. Burke

We present two examples that show how fusing data from hyperspectral imaging (HSI) sensors with data from other sensors can enhance overall detection and classification performance. The first example involves fusing HSI data with foliage-penetration synthetic aperture radar (FOPEN SAR) data; the second example involves fusing HSI data with high-resolution imaging (HRI) data. The fusion of HSI and SAR data exploits different phenomenology from the two different sensors. The fusion of HSI and HRI data combines their superior respective spectral and spatial information. Fusion of HSI and SAR data is accomplished at the feature level. HSI data provide background characterization and material identification; HSI-SAR fusion allows us to reduce false detections and confirm target detection in the SAR image. Fusion of HSI and HRI data is implemented at both data and feature levels, resulting in a combined spatial-spectral analysis that enhances target identification.

Hyperspectral imaging (HSI) sensors collect data that can be represented by a three-dimensional data cube. The hyperspectral data cube is resolved in along-track, cross-track, and spectral dimensions. The HSI sensor affords fine spectral resolutions ($\Delta\lambda \sim 10$ nm), typically in the visible to shortwave infrared (SWIR) wavelength region (0.4 to 2.5 μm). For each pixel within a hyperspectral image, a continuous spectrum is sampled and can be used to identify materials by their reflectance. One shortcoming of HSI is that it provides no surface penetration. Another shortcoming is that HSI spatial resolutions are usually coarser than those from panchromatic imagery. (The article in this issue entitled "Spectral Imaging for Remote Sensing," by Gary A. Shaw and Hsaio-hua K. Burke, discusses the interplay between spectral and spatial resolution.)

To overcome these limitations and enhance HSI system performance, we fuse HSI data with other sensor data. For example, in counter camouflage, concealment, and deception (CC&D) applications, HSI data can be used to identify ground cover and surface material, and a low-frequency foliage-penetration synthetic aperture radar (FOPEN SAR) can determine if any threat objects are under concealment. The sidebar entitled "Foliage-Penetration Synthetic Aperture Radar" explains the fundamentals of this technology and how Lincoln Laboratory has supported its development.

Because FOPEN SAR and HSI sensors exploit different phenomenology, their detection capabilities complement each other. FOPEN SAR typically operates at 20 to 700 MHz. It penetrates foliage and detects targets under tree canopy, but has significant clutter returns from trees. HSI, on the other hand, is capable of subpixel detection and material identification. Both SAR and HSI systems may suffer substantial false-alarm and missed detection rates because of

FOLIAGE-PENETRATION SYNTHETIC APERTURE RADAR

THE FOLIAGE-PENETRATION synthetic aperture radar (FOPEN SAR) was developed to find stationary tactical targets located in deep foliage and natural camouflage that cannot be penetrated by conventional microwave or electro-optical sensors. During the Vietnam War era, military personnel successfully used the Camp Sentinel ground-based radar to detect enemy soldiers and vehicles moving in foliage. To locate stationary targets, researchers needed to develop a low-frequency FOPEN SAR imaging capability with sufficient resolution to differentiate targets from clutter. Unfortunately, no reliable target-recognition algorithms were available at that time to reduce false alarms. Many of the successful automatic-target-recognition and cueing techniques for detecting moving and stationary targets were developed only for targets in the open.

Since the late 1980s, Lincoln Laboratory, under sponsorship by the Defense Advanced Research Projects Agency (DARPA) and the U.S. Air Force, has planned and conducted several experiments and data-collection programs with a variety of industry-built sensors to evaluate the use of low-frequency radar to detect and identify tactical targets hidden by foliage. The results from these efforts have been used to develop the current automatic-target-detection and cueing algorithms that operate on UHF and VHF SAR data. When we use a SAR system to detect objects obscured by foliage, detection is degraded in three ways for higher microwave frequencies (>100 MHz). First, the foliage contributes to the clutter return. Second, the foliage attenuates signal propagation through it. Third, moving foliage induces fluctuations in the amplitude and phase of the radar signal, which distort the SAR image of the target. These fluctuations affect the image-focusing quality and the detection performance of SAR.

To better understand foliage

their respective background clutter, but we expect that combining SAR and HSI data will greatly enhance detection and identification performance.

Another opportunity for HSI data fusion occurs in surface surveillance of exposed targets. Unlike conventional single-band or multispectral sensors, HSI sensors collect image data in hundreds of contiguous narrow spectral bands with only moderate spatial resolutions. By spatially sharpening a hyperspectral image with a panchromatic high-resolution image, we can enhance image visualization for the analyst. Such a combination of sensors can be found, for example, on the National Aeronautic and Space Administration's Earth Observing (EO)-1 satellite, which was launched in November 2000. This satellite includes an HSI sensor, Hyperion, and a high-resolution imaging (HRI) sensor as part of the Advanced Land Imager. The HRI sensor spatial resolution of 10 m is three times better than that of the HSI sensor.

In the next section, we describe an example of HSI-SAR fusion. Because HSI and SAR sensors are distinct and exploit different phenomenology, fusion of HSI and SAR data is established at the level of features such as material composition and terrain type. We then explore HSI-HRI data fusion. HSI sharpening with HRI data is first investigated. A combined spatial-spectral analysis is then discussed to illustrate enhanced target detection and identification.

HSI and FOPEN SAR Data Fusion

In May 1997 a P-3 ultrawideband (UWB) radar, operating from 215 to 730 MHz, and a Hyperspectral Digital Imagery Collection Experiment (HYDICE) sensor, operating from 0.4 to 2.5 μm in 210 bands, collected data at a site in Vicksburg, Mississippi. The SAR data were collected with a 32° depression angle effects, researchers needed an accurate quantitative assessment of these issues. In 1990, Lincoln Laboratory conducted a definitive experiment to measure foliage attenuation and backscatter of heavily forested areas. This experiment was conducted with the NASA–Jet Propulsion Laboratory Airborne SAR (AIRSAR) aircraft, which has UHF, L-band, and C-band SAR radars.

In the past decade, this FOPEN work has been extended to develop a phenomenological understanding of foliage penetration and to develop advanced automatic-target-detection and recognition techniques. Additional foliage-penetration measurements were made in 1993 in tropical rain forest and northern U.S. forest environments. In these measurements, the Swedish 3-m-resolution Coherent All Radio Band Sensor (CARABAS) and the Stanford Research Institute ultra wideband (UWB) SAR sensor collected horizontal-polarization VHF and UHF data. Foliage-induced attenuation for all frequency bands was calculated by comparison of echoes from test reflectors in foliage with those in the open. In support of the DARPA-sponsored FOPEN SAR project, Lincoln Laboratory has developed automatic-target-detection and cueing algorithms for VHF and UHF radar. With the detection of targets now possible with our existing foliage-penetration capability, the remaining issue becomes discriminating the threatening targets from all of the many detections that are reported. Two false-alarm mitigation techniques, change detection and group detection, have been used to reduce false alarms substantially.

Recently, many researchers have become interested in the use of AIRSAR for detection of underground targets, large and small, such as mines and trucks hidden in underground bunkers. Under the sponsorship of DARPA, the U.S. Army, and the U.S. Air Force, research into this application has led to the FOPEN Advanced Technology Demonstration system being built by Lockheed Martin Space Systems Company (LMSC).

Reference

1. T.G. Bryant, G.B. Morse, L.M. Novak, and J.C. Henry, "Tactical Radars for Ground Surveillance," *Linc. Lab. J.* **12** (2), 2000, pp. 341–354.

and a ground sample distance (GSD) of 0.23 m × 0.4 m. The HSI data were collected at a 1.5-km altitude with a nadir viewing geometry and GSD of 0.76 m × 1.1 m. These measurements formed part of the Dixie-97 data set that we use here to demonstrate the framework of HSI-SAR data fusion.

Figure 1 shows a sketch of the target site and the composite data set, including a hyperspectral data cube and a SAR grayscale image. Targets in the forest background include fabric nets and vehicles. Several fabric nets are placed along the tree line around an open area. One fabric net at the tree line covers a vehicle; all other nets are empty or cover nonradar reflecting decoys. One vehicle is obscured at the lower right corner of the sketch and another vehicle is partially exposed near the top left corner.

For the Dixie-97 data, a HSI-SAR fusion strategy was established on the basis of each sensor's detection characteristics. HSI and SAR data were first processed separately for detection and terrain classification, respectively. Then coregistration was performed to allow overlay of the images. Terrain mapping reduced SAR false alarms from trees. Detection of concealed targets under nets was verified and detection of partially exposed targets was further confirmed with material identification by HSI. We provide an analysis of the HSI data first, followed by an example of SAR-HSI image coregistration and the data fusion results.

HSI Data Analysis

Sample spectra of backgrounds of road, grass, trees, and nets are plotted as a function of wavelength in Figure 2. The road spectrum is significantly higher than other spectra in the visible wavelength region from 0.4 to 0.7 μm. The spectra for grass and trees each exhibit a decrease of reflectance at 0.68 μm, fol-

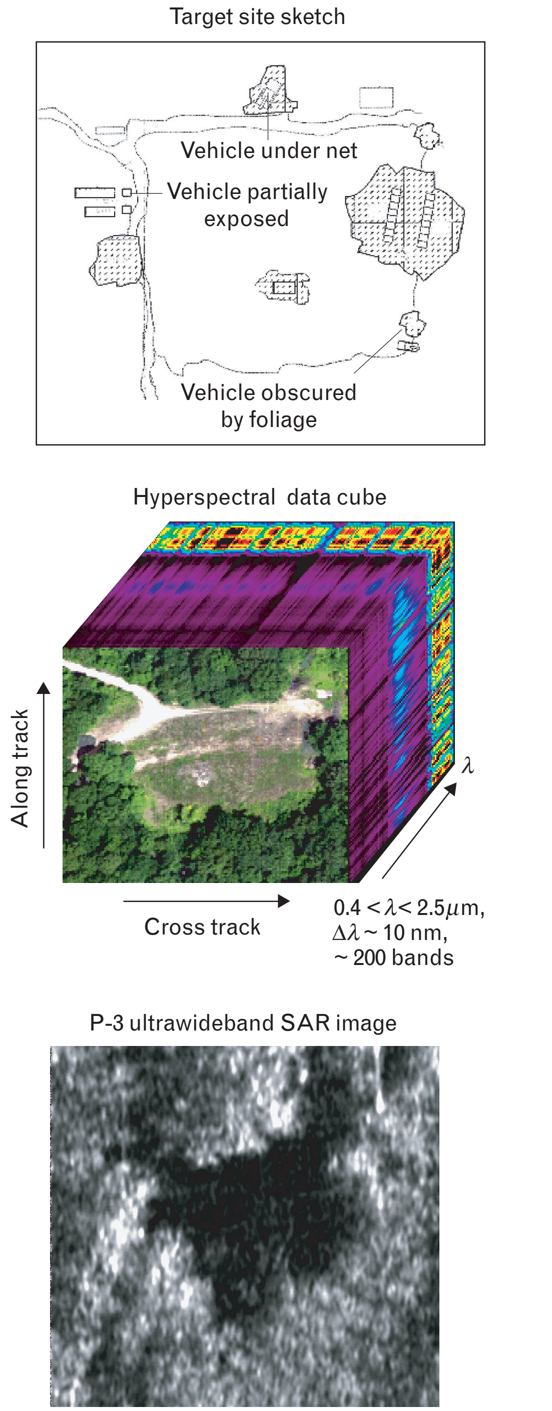

FIGURE 1. Target site sketch (top), hyperspectral data cube (middle), and synthetic aperture radar (SAR) data (bottom), part of the Dixie-97 data set. The site sketch shows targets in a forest background of fabric nets and vehicles. Several nets are placed along the tree line around an open area. One net at the tree line covers a vehicle. The hyperspectral data are displayed as a cube with a red-green-blue composite image on the front face. The SAR data are displayed as a radar-cross-section image in grayscale.

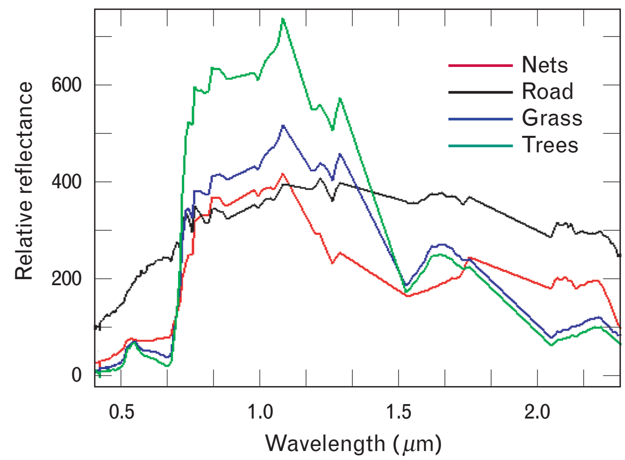

FIGURE 2. Sample spectra from a forest scene. The road spectrum is significantly higher than other spectra in the visible wavelength region of 0.4 to 0.7 μm. The spectra for grass and trees each exhibit decreased reflectance at 0.68 μm followed by a large increase at near infrared because green plants use chlorophyll to reflect infrared radiation and absorb the visible light from the sun.

lowed by a large increase at near infrared, characteristic of vegetation, because the chlorophyll in green plants absorbs the visible light from the sun and reflects the infrared radiation. In the SWIR wavelength region, spectral signatures of road and nets differ from the vegetation signatures.

Reduction in spectral dimensionality is first applied to the HSI data cube to extract the spectral features that then lead to further analysis. Principal-component analysis is used to decorrelate data and maximize the information content in a reduced number of features [2]. The sidebar entitled "Principal-Component Analysis" explains the mathematical foundation and applications of this technique.

Figure 3 shows sample principal components calculated from the Dixie-97 HSI data. Background classes of open area, trees, and roads are apparent in the first and third principal components; fabric nets appear in strong contrast to the backgrounds in the seventh principal component. We constructed a matched filter from the mean of several pixels extracted from the nets. A matched-filtering algorithm with thresholding was then applied to the HSI data to detect all pixels of fabric nets. Figure 4 shows the fabric-net detection and a color-coded terrain classifica-

PRINCIPAL-COMPONENT ANALYSIS

MULTISPECTRAL AND hyperspectral images can be spectrally transformed to generate new sets of image components. The transformed image can make features evident that are not discernible in the original data. Alternatively, it might be possible to preserve the essential information content of the image with a reduced number of the transformed dimensions.

Principal-component analysis uses a linear transformation, the principal-components transform, to translate and rotate multiband spectral data into a new coordinate system. This transform is also known as the Karhunen-Loève, or Hotelling, transform. Principal-component analysis is used to decorrelate data and maximize the information content in a reduced number of features. The covariance matrix is first computed over the pixel spectra contained in the hyperspectral data cube of interest. Eigenvalues and eigenvectors are then obtained for the covariance matrix Γ as given below:

$$\begin{aligned}\Gamma_x &= E\{(\mathbf{x} - \mu_x)(\mathbf{x} - \mu_x)^T\} \\ &= \Phi\Sigma\Phi^T ,\end{aligned}$$

where $\mathbf{x}$ is the spectral vector data, μ_x is the mean spectral vector over the data cube, E is the average operator over the entire data cube, Φ is a matrix consisting of columns of eigenvectors, and Σ is a diagonal matrix of eigenvalues.

We use the eigenvectors as a new coordinate system to transform the hyperspectral data cube into principal components, also called eigenimages.

If the transformed spectral data $\mathbf{x}$ is represented as $\mathbf{y}$ in the new coordinate system, then the principal-component transformation is a linear transformation Φ^T of the original coordinates, such that

$$\mathbf{y} = \Phi^T \mathbf{x} .$$

In y space the covariance matrix is given as

$$\Gamma_y = E\{(\mathbf{y} - \mu_y)(\mathbf{y} - \mu_y)^T\} ,$$

where μ_y is the mean vector expressed in terms of the y coordinates. A property of the transform is that

$$\mu_y = \Phi^T \mu_x .$$

As a result, Γ_y is the diagonal matrix of eigenvalues of Γ_x such that

$$\begin{aligned}\Gamma_y &= E\{(\Phi^T\mathbf{x} - \Phi^T\mu_x) \\ &\quad \times (\Phi^T\mathbf{x} - \Phi^T\mu_x)^T\} \\ &= \Phi^T E\{(\mathbf{x} - \mu_x)(\mathbf{x} - \mu_x)^T\}\Phi \\ &= \Sigma .\end{aligned}$$

Because Γ_y is a covariance matrix and is diagonal, its elements represent the variances of a set of orthogonal images in the transformed coordinate space. The eigenvectors are arranged in descending order of the eigenvalues so that the data exhibit maximum variance in the first component, the next largest variance in the second component, and so on, with the minimum variance in the last component.

In the case of hyperspectral and multispectral image data, image information is aggregated in leading principal components associated with large eigenvalues, and noises are segregated in trailing components associated with small eigenvalues. Thus principal-component analysis allows for the determination of the inherent dimensionality and segregation of noise components of the hyperspectral data. Singular value decomposition is a related transform concept that can be applied to a general matrix, including a non-square matrix, in order to decompose an image into orthogonal and basis images.

Reference

1. J.A. Richards, *Remote Sensing Digital Image Analysis: An Introduction,* 2nd ed. (Springer-Verlag, Berlin, 1993).

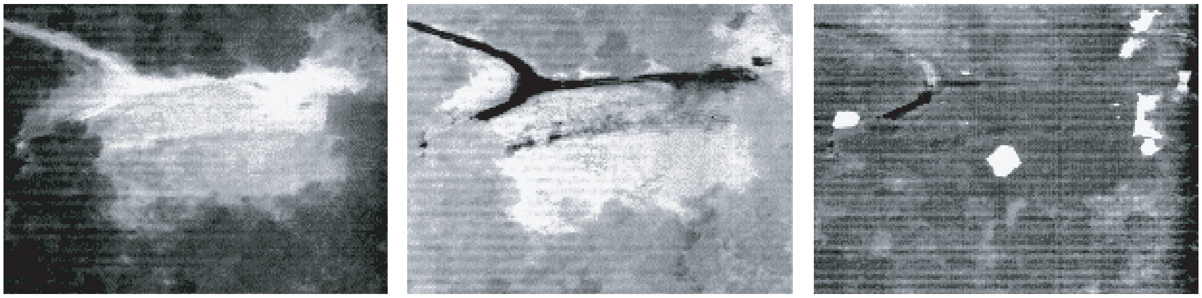

FIGURE 3. Principal components calculated from the Dixie-97 HSI data. Background classes of open area, trees, and roads are apparent in the first and third principal components. Fabric nets appear in strong contrast to the backgrounds in the seventh principal component.

tion map for the Dixie-97 HSI data. Superimposed on the terrain classification map is the HSI fabric-net detection. The map shows background classes for roads, grass, trees, and shadow regions; these classes result from an unsupervised data-clustering operation that uses the first five principal components.

Combined FOPEN SAR-HSI Analysis and Fusion

To combine HSI and SAR detection results, we performed coregistration with reference to terrain classes, such as open areas and trees, by using scaling, rotation, and translation operations. We then fused the data by using the coregistered images according to the process illustrated in Figure 5. The SAR data were first processed with pixel grouping and thresholding. The sample SAR detection at a 6-dBsm threshold is shown in the top left image of Figure 5. The detection of a near vertical line in the top right area of this SAR image corresponds to a power line. The terrain map derived from the HYDICE HSI data with open-area and fabric-net detections is the top middle image of Figure 5. In combining these analyses, we retained SAR detections only from open areas or around fabric nets indicated in the HSI data. Detections that coincided with HSI identifications of trees, far-from-open areas, and nets were considered false alarms. In the combined detection result, shown in the top right image of Figure 5, a SAR detection of a vehicle under a net appears; other nets are empty with no SAR detections. There are several strong SAR detections at the left side of the open area. A spectral angle map (SAM) algorithm was applied to match HSI data in the open area to paints in our spectral library. Three pixels matched well with military gray-tan paint. This

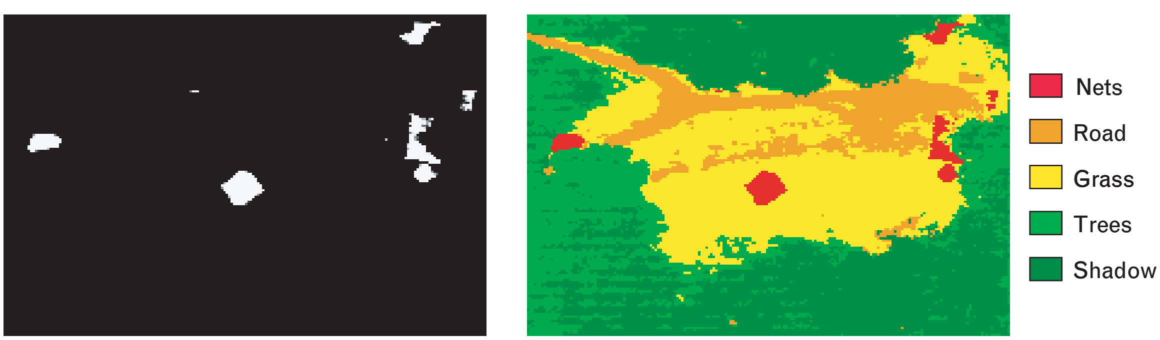

FIGURE 4. HSI fabric-net detection with a matched-filtering algorithm (left) and terrain classification map (right). The HSI fabric-net detection has been superimposed on the terrain classification map. Roads, grass, trees, and shadow regions are shown as separate terrain classes. These background classes result from an unsupervised data-clustering operation that uses the first five principal components.

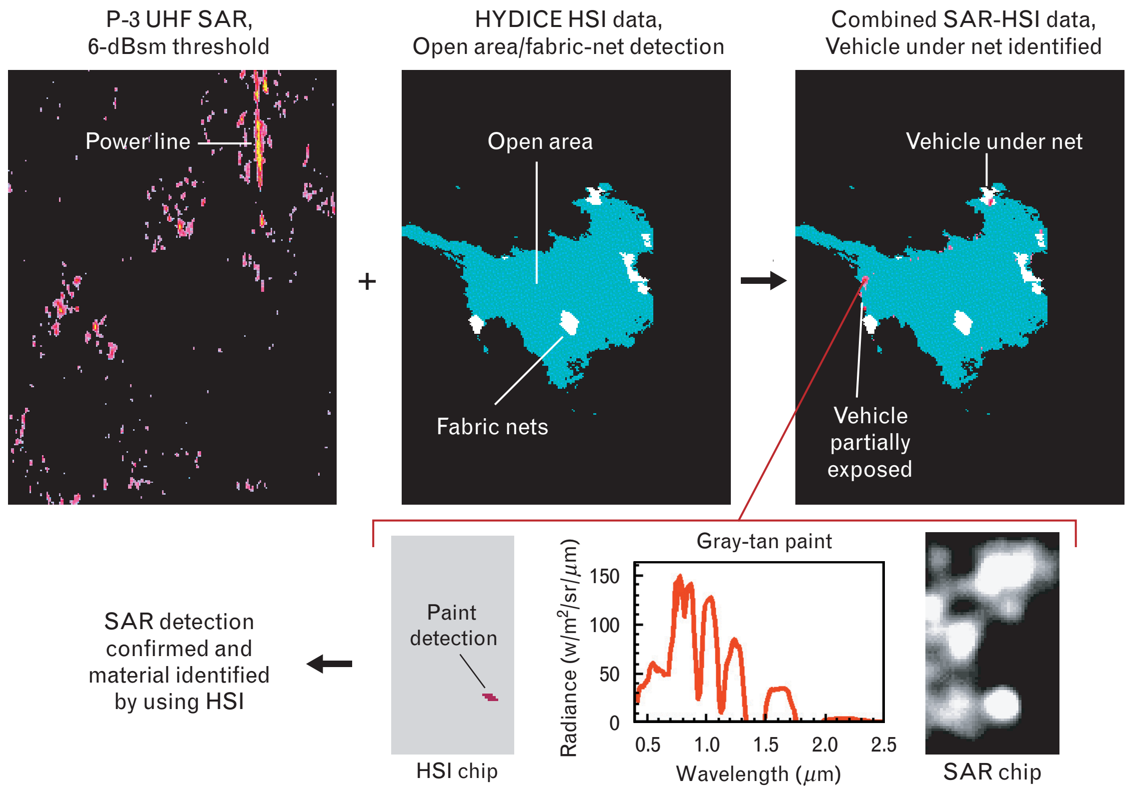

FIGURE 5. SAR detection (top left), a terrain map derived from the Hyperspectral Digital Imagery Collection Experiment (HYDICE) HSI data with net detections (top middle), and the combined detection result (top right). The SAR data were first processed with pixel grouping and thresholding. The sample SAR detection shows the detection of a vertical line in the top right area that corresponds to a power line. When we combined the analyses, only SAR detections from either open areas or around fabric nets indicated in the HSI data were retained. SAR detections that corresponded to identifications of trees, far-from-open areas, or nets on the hyperspectral image were considered false alarms. In the combined SAR-HSI data, a SAR vehicle detection appears under a net at the top right corner. Other nets detected in the HSI data are considered empty because they have no corresponding SAR detections. There are several strong SAR detections on the left side of the open area. A spectral angle map (SAM) algorithm was applied to match the HSI data in the area to paints in our spectral library. Three pixels match well with military gray-tan paint, indicating the presence of a vehicle, possibly military; this match confirms the SAR detection.

match indicated the presence of a vehicle, possibly military, in the open area and thus confirms the SAR detection.

HSI and HRI Data Fusion

To assess the fusion of HSI and HRI data, we generated a set of coregistered HSI and HRI data with known ground truth. We used the first frame of Hyperspectral Digital Imagery Collection Experiment (HYDICE) data from Forest Radiance I Run 05 as the "truth" in both spatial and spectral domains; it has 320 × 320 pixels and 0.8-m pixel resolution. The truth data were processed to generate simulated HSI (4 m/pixel, $\Delta\lambda \sim 10$ nm) and HRI (0.8 m/pixel, panchromatic) data. The simulated HSI data were generated by a 5 × 5 spatial averaging of the input data followed by a 5 × 5-to-1 undersampling. The resulting HSI image is 64 × 64 pixels in size with 4-m pixel resolution. The simulated HRI data were generated with a 25-band integration, from 0.63 μm to 0.9 μm, and $\Delta\lambda \sim 10$ nm, resulting in a 320 × 320 single-band image with 0.8-m pixel resolution. Figure 6 shows the flow of data generation for HSI and HRI fusion. In the following section, we first apply sharpening to the HSI data and then conduct a combined spatial-spectral analysis.

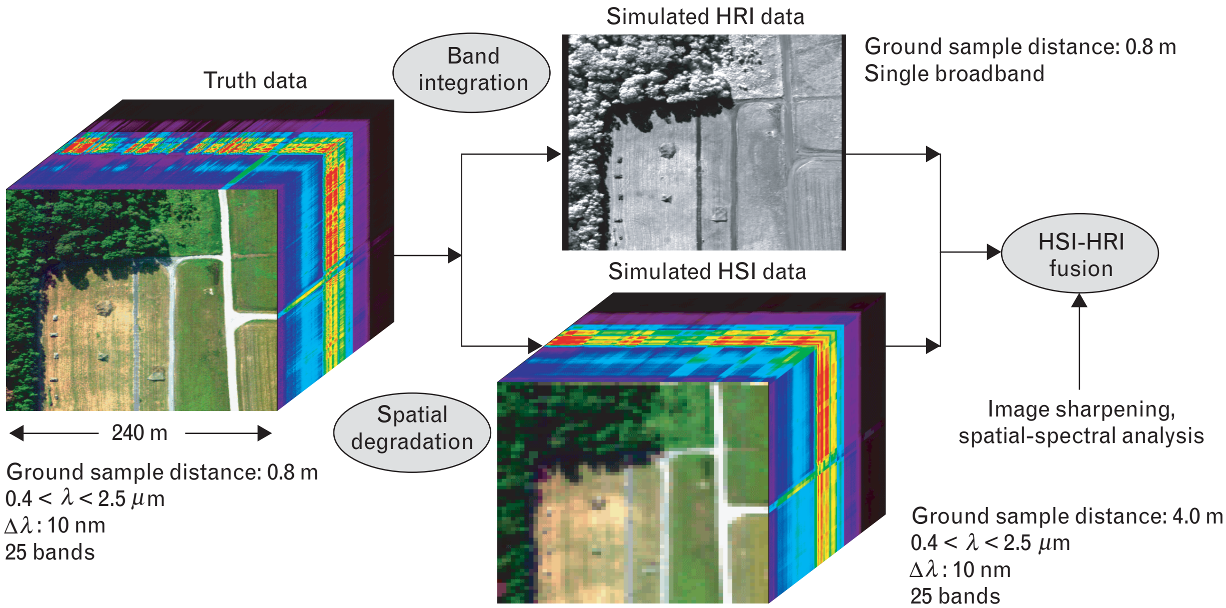

FIGURE 6. Flow of simulated data generation from the HSI truth data for HSI and High Resolution Imaging (HRI) data fusion. The first frame of HYDICE data from Forest Radiance I Run 05 is used as the truth in both spatial and spectral domains; it has 320 × 320 pixels, 0.8 m per pixel. The truth data are processed to generate the simulated HSI (4m/pixel, $\Delta\lambda \sim 10$ nm) and HRI (0.8m/pixel, panchromatic) data. The simulated HSI data are generated by a 5 × 5 spatial averaging of the input data followed by a 5 × 5-to-1 undersampling. The resulting hyperspectral data cube has 25 bands; each band is 64 × 64 pixels in size and 4 m per pixel. The HRI data are generated with a 25-band integration from 0.63 μm to 0.9 μm, $\Delta\lambda \sim 10$ nm. The result is a 320 × 320 single-band image, 0.8 m per pixel.

Review and Demonstration of Sharpening Algorithms

A number of image sharpening techniques are often applied to multispectral images for visualization enhancement. This section reviews three of the commonly used sharpening algorithms—pseudo inverse, color normalization, and spatial-frequency correction—that are adapted for implementation on HSI data. We show the results of applying these algorithms to the generated HSI and HRI data for a sharpened HSI image. Spectral fidelity is evaluated by comparing the original and sharpened data.

Pseudo-Inverse Technique [3, 4]. Given a high-resolution image coregistered with a hyperspectral image, a system of equations can be established for the reconstruction of a sharpened, or high-spatial-resolution, hyperspectral image. The value at a pixel in the high-resolution image is the spectral average at the same pixel in the sharpened hyperspectral image. The spectral value at a pixel in the hyperspectral image is the pixel sum of the sharpened hyperspectral image within the GSD of the hyperspectral image in the same spectral band. If the sharpening ratio—the ratio of GSDs between unsharpened and sharpened images—is integer r and the number of spectral bands is K, then the number of equations for each hyperspectral image pixel is $r^2 + K$, and the number of unknowns for the sharpened hyperspectral image reconstruction is $r^2 \times K$. As the sharpening ratio and the number of spectral bands increase, the number of unknowns increases faster than the number of additional equations. The system of equations is generally underdetermined for a unique solution. Pseudo matrix-inversion algorithms with least mean squared (LMS) estimations are applied to obtain a solution for the fusion problem. This method is described in the following equations:

$$\mathbf{E} = \mathbf{A}^{\mathrm{T}}(\mathbf{A}\mathbf{A}^{\mathrm{T}})^{-1}\mathbf{w} ,$$

and

$$\mathbf{AE} = \mathbf{w} ,$$

where $\mathbf{E}$ is a $(K \cdot r^2) \times 1$ array containing K bands of $r \times r$ sharpened hyperspectral image pixels, $\mathbf{A}$ is a

$(K + r^2) \times (Kr^2)$ matrix of the system equation, $\mathbf{A}^T(\mathbf{A}\mathbf{A}^T)^{-1}$ is the pseudo inverse of $\mathbf{A}$, and $\mathbf{w}$ is a $(K + r^2) \times 1$ array of the HSI and HRI input values.

In this approach the high-resolution image needs to be in perfect registration with the hyperspectral image to establish the system of equations. The pseudo-inverse technique uses singular value decomposition to obtain an LMS solution for the system. Performed on a pixel-by-pixel basis, the pseudo-inverse technique is very time consuming. Also, the LMS estimations do not necessarily attain spectral information beyond that originally contained in the HSI data.

Sharpening Color Normalization (SCN) [5]. The color-normalization algorithm conventionally used in multispectral imaging is modified for HSI sharpening. The HSI data are first oversampled to the same pixel size as the HRI data. The algorithm multiplies each of the HSI bands by the HRI data and the resulting values are each normalized by the averaged HSI data over the spectral bands covered in the panchromatic range of HRI. This process is defined by the following equation:

$$\mathbf{SCN}_i = \frac{(\mathbf{HSI}_i \times \mathbf{HRI})}{(\mathbf{HSI})_P},$$

where $\mathbf{HSI}_i$ is an HSI band, $\mathbf{SCN}_i$ is the $\mathbf{HSI}_i$ sharpened by color normalization, and $(\mathbf{HSI})_P$ is band-averaged **HSI** over the **HRI** panchromatic wavelength range.

This approach is straightforward in merging the spatial contrast of HRI into spectral bands of HSI. The method also requires good HSI-HRI data registration. The sharpened HSI data appear visually sharper but do not contain more spectral information than the original HSI.

Spatial-Frequency Correction (SFC). Some sharpening approaches use wavelet transformations [6] that decompose images into different spatial-frequency scales. In spatial-frequency correction, the HSI data are first oversampled to the same pixel size as the HRI data. For each HSI band, the high-frequency components are replaced with components from the HRI data. The sharpened image is then obtained via inverse transformation of the modified spectra. In practice, two-dimensional (2-D) Fourier transformation can be applied for image spatial-frequency analysis. The sharpening process is described below:

$$\mathbf{SFC}_i = \mathbf{FFT}^{-1}\{\mathbf{FFT}(\mathbf{HSI}_i)_, \mathbf{FFT}(\mathbf{HRI})_{\mathrm{hi}}\},$$

where $\mathbf{SFC}_i$ is the sharpened $\mathbf{HSI}_i$, $\mathbf{FFT}(\mathbf{HSI}_i)$ represents the 2-D spatial frequency components of $\mathbf{HSI}_i$, and $\mathbf{FFT}(\mathbf{HRI})_{\mathrm{hi}}$ represents the high-frequency components in the 2-D spatial Fourier transform of the HRI data. The sharpened $\mathbf{HSI}_i$ is the inverse 2-D Fourier transform of $\mathbf{FFT}(\mathbf{HRI})$ with the central (low-frequency) portion replaced by $\mathbf{FFT}(\mathbf{HSI}_i)$.

In this approach, the spatial shift caused by imperfect HSI-HRI registration shows up as a phase shift in the frequency spectrum. Some loss of spectral quality is expected in the sharpened data.

Discussion of Performance. In the three sharpening approaches reviewed, we emphasize that good spatial registration between HSI and HRI data is required. For our purpose of spectral fidelity evaluation, we have perfect coregistration through the method used to generate the HSI and HRI data. Two measures, spectral angle and spectral distance (Euclidean distance), are used to evaluate the sharpening algorithms. These quantities are calculated as

$$\text{spectral angle}(\mathbf{x}_1, \mathbf{x}_2) = \cos^{-1}\left[\frac{\mathbf{x}_1 \cdot \mathbf{x}_2}{|\mathbf{x}_1||\mathbf{x}_2|}\right],$$

and

$$\text{spectral distance}(\mathbf{x}_1, \mathbf{x}_2) = |\mathbf{x}_1 - \mathbf{x}_2|,$$

where $\mathbf{x}_1$ and $\mathbf{x}_2$ are two multiband spectra.

A zero angle or zero distance represents a perfect match of two spectra. The sharpened images are compared to the truth data in terms of spectral angle and spectral distance. The spectral distance normalized by the pixel amplitude in the truth image is calculated for the fraction of spectral difference. The frame-averaged differences for the three sharpening algorithms are listed in Table 1. For comparison, the difference measurements from the unsharpened HSI data are also included in the table. The unsharpened 4-m resolution image data are five times oversampled to compare with the truth image data at 0.8-m resolution. The sharpened images improve significantly from the unsharpened HSI data in spectral distance, but show

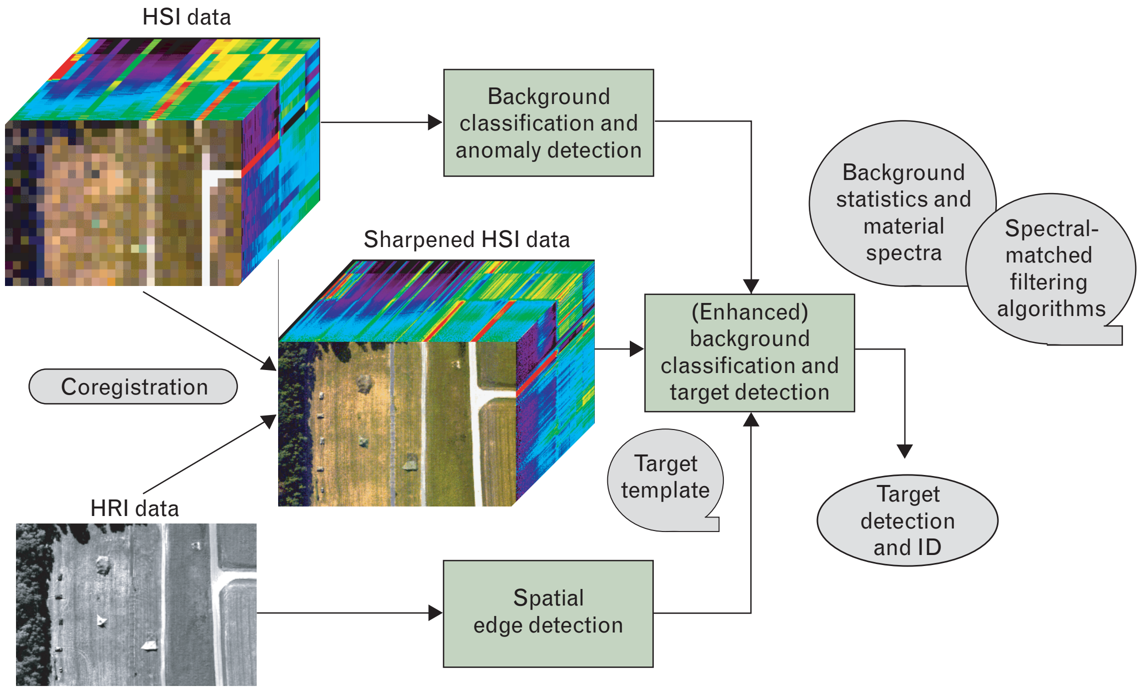

FIGURE 7. Diagram of a spatial-spectral analysis approach. Background classification and anomaly detection are first obtained from HSI data. Applying the results to the sharpened HSI data provides enhanced background classification and target detection, while the HRI data provide target and background boundaries with spatial edge detection. These edges, combined with results from the sharpened HSI data, spatially enhance the definition of targets and backgrounds. Finally, spectral-matched filtering for target detection is applied to the sharpened HSI data.

no obvious improvement in spectral angle. Among the sharpened images, color normalization is closer to the truth in spectral angle than to the results of pseudo-inverse and frequency correction. On the other hand, the spatial-frequency correction method achieves results that are closest to the truth in spectral distance.

Table 1. Sharpening-Algorithm Comparison with Respect to the Truth Data

	Spectral Angle	*Spectral Distance*
Unsharpened HSI data	4.9°	21.6%
Sharpened		
Pseudo inverse	8.3°	13.8%
Color normalization	3.8°	10.0%
Frequency correction	5.8°	8.2%

Although the sharpened images generally appear sharper, the impact of this effect is small on target detection and identification. Because the combined HSI-HRI data are severely underdetermined for the reconstruction of sharpened HSI data, spectral features of objects smaller than the original HSI resolution cannot be fully resolved in the sharpened HSI. Additional spatial and spectral analysis at the feature level is necessary for enhanced target detection and identification. In the spatial-spectral analysis discussion that follows, HSI data sharpened by color normalization will be used.

Spatial-Spectral Analysis

Various combinations of spatial and spectral analysis of HSI and HRI images have been attempted [7–9]. To demonstrate HSI-HRI fusion for enhanced background characterization and target detection-identifi-

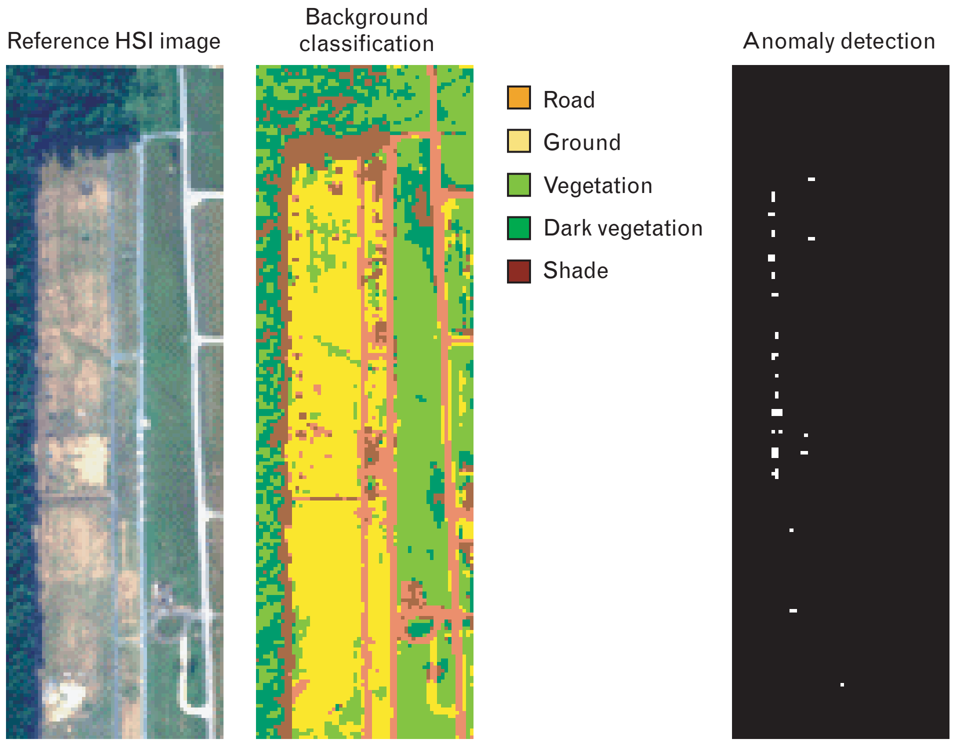

FIGURE 8. Reference HSI image (left), background classification (middle), and anomaly detection (right) derived from the unsharpened HSI data. The background classification is the result of an unsupervised data-clustering operation on the first five principal components. Road, ground, vegetation, and shade are delineated. The background map and class statistics are employed in all subsequent processing. Areas in the HSI reference image that do not match the background classification are considered anomalies, as shown on the right.

cation, we employ a similar combined spatial-spectral analysis. Figure 7 shows our analysis approach. We first obtain background classification and anomaly detection from HSI data. Applying these results to the sharpened HSI data provides enhanced background classification and target detection, while the HRI data provide target and background boundaries with spatial edge detection. These edges, combined with results from the sharpened HSI data, spatially enhance the definition of targets and backgrounds. After we apply spectral-matched filtering, the HSI data further reveal the background and target materials.

To illustrate this analysis approach, we used an expanded data set consisting of three major frames of HYDICE data from Forest Radiance I Run 05. The original truth image of 300 × 960 pixels, 0.8-m pixel resolution, and 210 bands was used as input. The degraded low-resolution hyperspectral image was 60 × 192 pixels in size, 4-m pixel resolution, and 210 bands. The corresponding HRI image was generated with band integration from 0.4 to 0.8 μm, 300 × 960 pixels, with 0.8 m pixel resolution. A sharpened hyperspectral data cube was obtained from the combined HSI and HRI data by using the color-normalization method.

Figure 8 shows a reference HSI image, as well as a background classification and anomaly-detection map derived from the unsharpened (4-m GSD) HSI data. The background classification is the result of an unsupervised data-clustering operation on the first five principal components [10]. Road, ground, vegetation, and shade are delineated. The background map and class statistics are employed in all subsequent processing. Areas in the hyperspectral reference image that do not match the background classification are considered anomalies; these anomalies are further processed with spatial and spectral analysis for

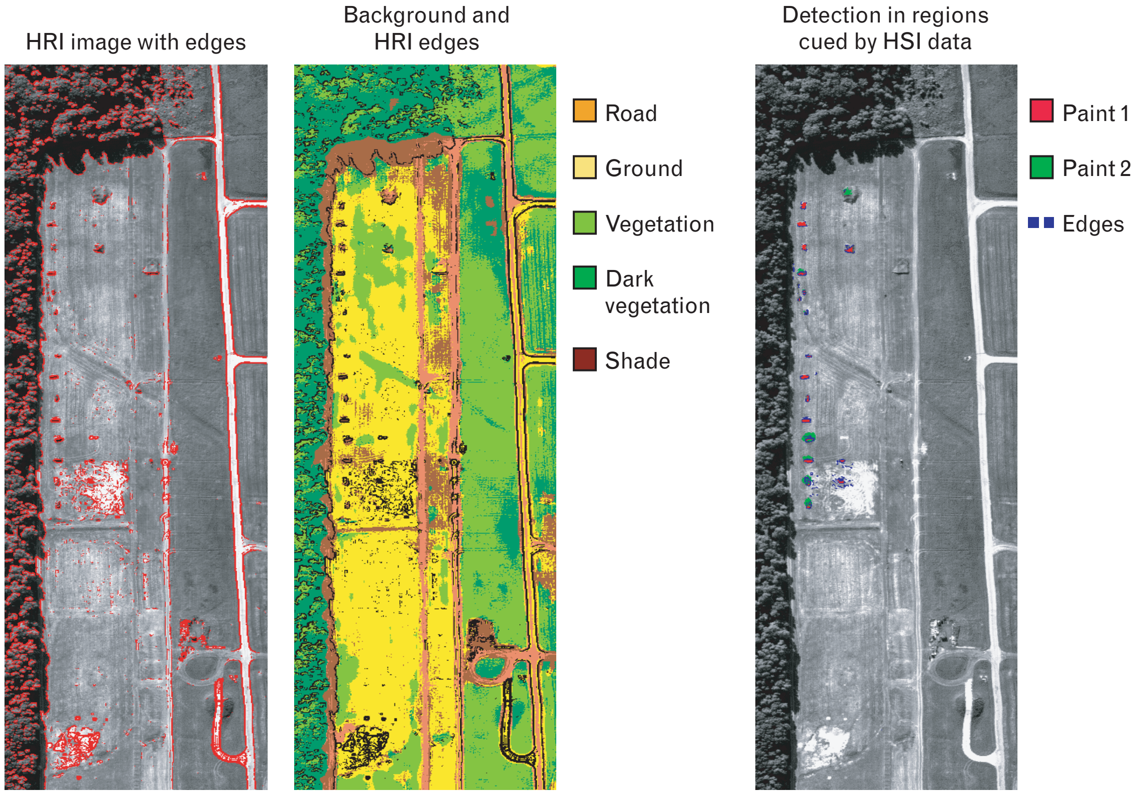

FIGURE 9. HRI image with detected edges (left); background classification from sharpened HSI data overlaid with HRI-derived edges (middle); and target detection on sharpened HSI data (right). Background boundaries in the sharpened HSI are enhanced with the edges derived from the HRI image. The image on the right depicts the combined results of spectral matched filtering and spatial edges over regions with anomaly detections from HSI. Red and green colors each represent different types of vehicle paints; the detections are bounded by the edges shown in blue.

target detection and identification. Edges detected from the HRI image with the Sobel operator [11] are shown in Figure 9. Overlay of the edges with background classification from sharpened HSI data is also shown in the figure. Background edges in the sharpened HSI data are enhanced with the edges derived from the HRI image. The image on the right of Figure 9 depicts the combined results of spectral-matched filtering and spatial edges over regions containing anomaly detections from HSI. In the far right grayscale image, red and green represent different types of vehicle paints, and the detections are bounded by the edges shown in blue. Two regions of detection located near the top of the scene, however, are not well defined in shape and appear to be large in size. These are inconsistent with vehicle features. Further testing with spectral matched filtering confirms pieces of fabric in these regions, as shown in Figure 10, which contains an enlarged view of the vehicle detections. The vehicle size and orientation can be determined from the bounding edges. Objects are classified as large vehicles (4 m × 8 m) if they are 4 to 7 pixels wide and 8 to 11 pixels long. Likewise, objects are small vehicles (3 m × 6 m), if they are 3 to 5 pixels wide and 6 to 7 pixels long. The colored bar next to each vehicle in the enlarged image depicts the vehicle's size, orientation, and paint type.

Summary and Discussion

Relative to previous multispectral sensors, HSI sensors offer superior spectral resolution that allows detailed background characterization and material-identification-related applications. These capabilities employed in conjunction with other remote sensing modalities can further enhance the combined system performance. The potential payoff of fusing HSI data with data from other sensors has been illustrated in this article. FOPEN SAR compensates for the lack of

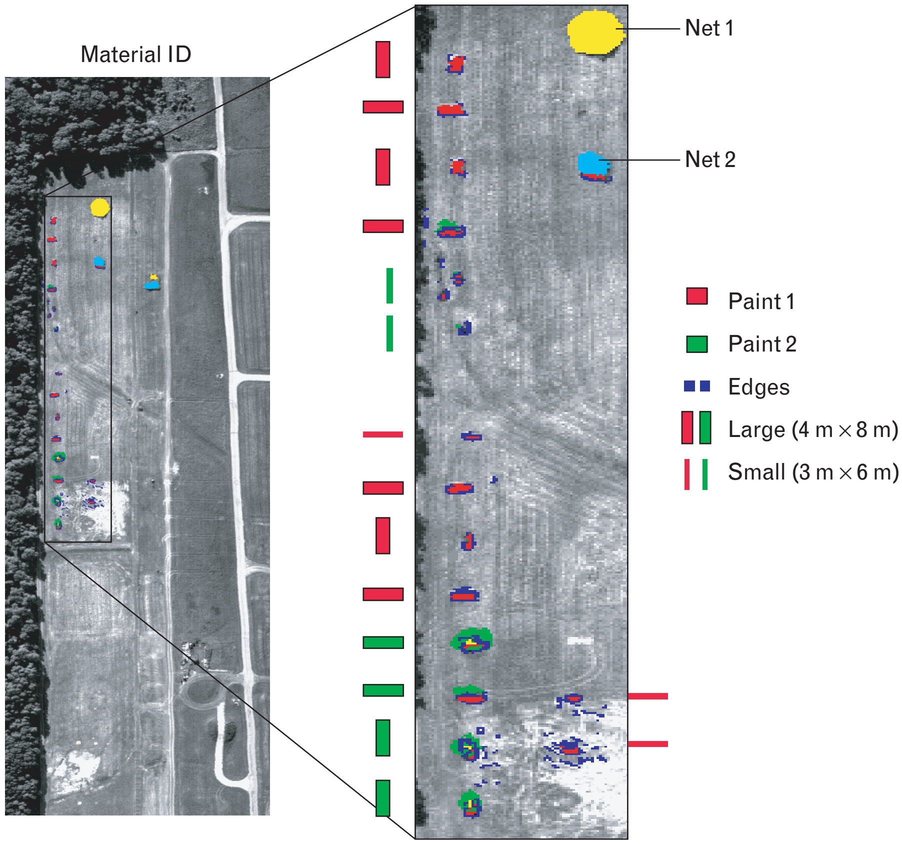

FIGURE 10. Fabric and additional object identification. An enlarged view of the vehicle detections is on the right. The vehicle size and orientation can be determined from the bounding edges. Objects are classified as large vehicles (4 m × 8 m) if they are 4 to 7 pixels wide and 8 to 11 pixels long. Likewise, objects are small vehicles (3 m × 6 m), if they are 3 to 5 pixels wide and 6 to 7 pixels long. The colored bar next to each vehicle in the enlarged image depicts the vehicle's size, orientation, and paint type.

surface penetration capability in HSI caused by the HSI sensor's passive sensing function. The fact that SAR and HSI sense different phenomena also helps in reducing false detections. HSI's other shortcoming is suboptimal spatial resolution due to the trade-off with fine spectral resolution. A panchromatic HRI image, typically with much better spatial resolution, provides additional spatial enhancement on target detection and background delineation derived from HSI data.

Coordinated data collection is required to demonstrate multisensor fusion performance. The platforms should be relatively stable and capable of georeferencing to allow multisensor coregistration for data fusion. For the purpose of algorithm development and assessment, spatial and spectral ground truth supporting all participating sensors is also required to fully realize the system performance. While there have been some multisensor data collections to date, they were typically focused on a single sensor rather than designed synergistically for multisensors. In general, these data are not optimally suited for data/image fusion demonstration. For the SAR-HSI fusion example we provided, coregistration was accomplished by manual selection of tie points over a small common area of SAR and HSI. Simulated data with perfect coregistration were used for the HSI and HRI fusion example.

In this article, we demonstrated the framework of HSI fusion with FOPEN SAR and HRI data by using various sources of data. P-3 SAR UWB data and HYDICE HSI data from the Dixie-97 data collection over Vicksburg, Mississippi, were used for SAR-HSI data fusion. Targets in the forest background of this data set included fabric nets and vehicles. Principal-component analysis on the HSI data was shown to allow effective spectral dimension reduction and feature extraction for terrain characterization and fabric-net detection. SAR-HSI feature fusion was accomplished with a coregistration of the images by using references to terrain features. The fusion results showed detection of a vehicle under a fabric net and reduction of SAR false alarms due to trees. A case of SAR detection was also confirmed by HSI material matching with military vehicle paint.

The Dixie-97 example demonstrates the UHF SAR's capability of penetration through nets. However, the detections come with significant false alarms from trees. Background classification and anomaly detection from HSI data reduce SAR false alarms in target detection, as illustrated in the Dixie-97 example. Additional target processing of UHF SAR data with template matching and HSI material identification will both enhance target detection and reduce false alarms.

For HSI-HRI data fusion, sharpening approaches were investigated and implemented on a combined HSI and HRI data set. The sharpened hyperspectral image retained the spectral signatures of the extended area and in general appeared visually sharper. Spectral features of objects smaller than the original HSI resolution, however, were not fully resolved through sharpening, due to the underdetermined nature of the reconstruction of the sharpened HSI. Thus the utility of sharpening alone is limited. Further analysis was conducted to combine respective high-spectral and high-spatial resolution information from HSI and HRI data; this HSI-HRI fusion demonstrated enhanced background characterization as well as target detection and identification performance. Anomalies detected from HSI data were used to cue for target detection and identification in the combined analysis. Spatial image processing was applied to HRI for edge delineation. As the result of combined analysis, target size, shape, and material were determined.

REFERENCES

1. L.J. Rickard, R. Basedow, E. Zalewski P. Silvergate, and M. Landers, "HYDICE: An Airborne System for Hyperspectral Imaging," *SPIE* **1937**, 1993, pp. 173–179.
2. J.R. Schott, *Remote Sensing: The Image Chain Approach* (Oxford University Press, New York, 1997).
3. T.J. Patterson and M.E. Bullock, "Radiometrically Correct Sharpening of Multispectral Images Using a Panchromatic Image," *SPIE* **2234**, 1994, pp. 252–264.
4. T.J. Patterson, L. Gong, R. Haxton, and T. Chinen, "Extension of Sharpening Techniques to Hyperspectral Data," *SPIE* **3372**, 1998, pp. 114–122.
5. J. Vrabel, "Advanced Band Sharpening Study," *SPIE* **3071**, 1997, pp. 73–84,
6. M.A. Goforth, "Multispectral Image Sharpening with Multiresolution Analysis and the MTF," *SPIE* **3372**, 1998, pp. 123–131.
7. H.N. Gross and J.R. Schott, "Application of Spatial Resolution Enhancement and Spectral Mixture Analysis to Hyperspectral Images," *SPIE* **2821**, 1996, pp. 30–41.
8. H.N. Gross and J.R. Schott, "Application of Spectral Mixture Analysis and Image Fusion Techniques for Image Sharpening," *Rem. Sens. Environ.* **63** (2), 1998, pp. 85–94.
9. B. Zhang, J. Liu, X. Wang, and C. Wu, "Study on the Classification of Hyperspectral Data in Urban Area," *SPIE* **3502**, 1998, pp. 169–172.
10. R.A. Schowengerdt, *Remote Sensing, Models and Methods for Image Processing* (Academic Press, San Diego, 1997).
11. R. Gonzalez and P. Wintz, *Digital Image Processing*, 2nd ed. (Addison-Wesley, Reading, Mass., 1987).

SU MAY HSU
is a staff member in the Sensor Technology and System Applications group. She researches hyperspectral image data analysis, focusing on background classification, target detection, and sensor fusion applications. Before joining Lincoln Laboratory in 1981, Su May worked in image data analysis for the General Electric Company in Schenectady, New York. She holds a B.S. degree from the National Taiwan University and a Ph.D. degree from Purdue University, both in electrical engineering.

HSIAO-HUA K. BURKE
leads the Sensor Technology and System Applications group at Lincoln Laboratory. In the area of remote sensing, she specializes in applications of optical sensors, particularly data analysis and algorithm development. A recent area of interest is the application of hyperspectral technology to Department of Defense needs, including fusion of hyperspectral data information with other sensors. She received her Ph.D. degree in atmospheric physics from Rice University, and joined Lincoln Laboratory as a staff member in 1981.